In situ investigation of the Columnar-to-Equiaxed Transition during directional solidification of Al–20 wt.%Cu alloys on Earth and in microgravity

F. Ngomesse, G. Reinhart, H. Soltani, G. Zimmermann, D.J. J Browne, W. Sillekens, H. Nguyen-Thi

In situ investigation of the Columnar-to-Equiaxed Transition during directional solidification of Al–20wt.%Cu alloys on Earth and in microgravity

F. Ngomesse[1], G. Reinhart[1], H. Soltani[2], G. Zimmermann[3], D.J. Browne[4], W. Sillekens[5], H. Nguyen-Thi[1]

[1] Aix Marseille Univ, Université de Toulon, CNRS, IM2NP, Marseille, France

[2] Badji Mokhtar University, LMGM, BP 12, 23000, Annaba, Algeria

[3]ACCESS e.V., Intzestr. 5, 52072 Aachen, Germany

[4]School of Mechanical and Materials Engineering, University College Dublin, Belfield, Dublin 4, Ireland

[5] European Space Agency – ESTEC, Keplerlaan 1 Postbus 299, 2200 AG Noordwijk, The Netherlands

Abstract

Solidification experiments on Al–20wt.%Cu alloys with grain refiner were performed in a Bridgman-type furnace to investigate the impact of gravity-driven phenomena on the Columnar-to-Equiaxed Transition (CET) during directional solidification *(i)* in microgravity, on board the sounding rocket MASER-14 and *(ii)* on Earth in three growth directions, namely horizontal, vertical upward (counter-gravity direction) and vertical downward (in-gravity

direction). The CET was provoked by a step increase of the cooling rate and was visualised *in situ* and in real-time using X-radiography. This paper reports direct observations of dendritic columnar growth, CET and the subsequent equiaxed regime, and quantitative characterisation of the microstructures. The increase in constitutional undercooling that induces the nucleation of the first grains ahead of the columnar front can be related to the rapid thermal change following the increase in cooling rate. The nucleation distance of equiaxed grains ahead of the columnar front is larger in microgravity than on Earth and possible origins for this difference are discussed. Both mechanical and solutal blocking mechanisms were observed at CET. Mechanical blocking is attributed to the occurrence of solidification-induced shrinkage flow. The relative importance of each blocking mechanism is detailed for each growth configuration. In particular, mechanical blocking is shown to be the principal type of impingement in the microgravity experiment. The final equiaxed grain structure was characterised, and the results confirm that gravity effects become less significant at high growth rates.

Keywords: Microgravity, directional solidification; Columnar-to-Equiaxed Transition, grain characteristics, *in situ* X-radiography; Al-Cu alloy, gravity, convection

1. Introduction

The properties of metallic alloys are directly related to their solidification microstructures so a detailed understanding of nucleation and growth processes is of tremendous importance in

engineering [1]. During industrial processes such as ingot casting, welding or additive manufacturing, the formation of two types of microstructure is usually observed depending on the solidification parameters (temperature gradient, cooling rate, alloy composition): the columnar structure giving rise to directional properties, and the equiaxed structure with more uniform and isotropic properties [2]. The columnar grain structure is required for instance for aerospace turbine blades, while equiaxed grains are desired for automotive applications such as car engines or suspensions. Equiaxed growth can be promoted by adding small particles known as inoculants, which act as seeds to promote heterogeneous nucleation. During industrial processes, a transition between those two types of grain structure is often observed: it is the Columnar-to-Equiaxed Transition (CET). It is usually induced by an increase of the solidification velocity or a decrease of the temperature gradient during the solidification process [2]. This transition occurs when the columnar front is blocked by equiaxed grains, either by hard blocking when equiaxed grains become in direct contact with the columnar front, or by soft blocking when solutal or thermal interactions between equiaxed grains and the columnar front cause the progressive deceleration of the columnar front and eventually its halt [3]. CET can be sharp, leading to two distinct parts in the material with dramatically different properties, or progressive, with the co-existence of both columnar and equiaxed structures [4–6]. It is worth noting that the relative importance of each impingement mechanism for CET (hard vs. soft) is still unclear, especially due to the lack of reference experiments using *in situ* observations to investigate this topic.

On Earth, gravity is the cause of many phenomena that make the understanding of the solidification process, and specifically the CET, difficult. Firstly, natural convection occurring in the melt significantly affects the mechanism of heat and mass transport [7] and can thus modify the position of the CET [6]. Another effect of gravity is buoyancy that gives rise to the sedimentation or the flotation of solid grains [8,9], which can highly participate to or influence the CET. Also, buoyancy leads to mechanical effects such as dendrites bending [10], which can help to promote fragmentation and cause CET if the dendrite fragments are transported ahead of the solidification front by fluid flow. Recently, variation of hydrostatic pressure by changing the gravity level has also been highlighted as an effect that can modify the microstructure [11] and cause CET [12]. To reduce such effects on the microstructure formation, thin alloy samples and horizontal solidification can be used [13,14]. Nevertheless, gravity effects still exist even in the latter configuration. Therefore, microgravity experimentation is the method of choice since gravity effects are almost eliminated in such an environment and solidification experiments can be carried out in nearly diffusive regime [15]. Benchmark data can thus be obtained for the improvement of numerical studies [16] and comparative study between experiments on Earth and in microgravity can be achieved to enlighten gravity effects [17,18].

Over the last couple of decades, X-radiography has become a relevant technique to investigate microstructure formation dynamics in metal alloy solidification [19], and especially gravity-induced effects [20–22]. For such studies, synchrotron sources are mainly used because they provide a continuous range of photon energies and an intense X-ray beam [23]. However,

the synchrotron X-ray beam is horizontal, which constrains solidification experiments to a vertical configuration (upward and downward growth), where gravity effects are expected to be strong. Recent developments made compact microfocus X-ray sources, X-ray sensitive cameras and optics more efficient, allowing home laboratory alternatives with substantial brilliance to be used [13,24,25]. Solidification experiments could then be performed on ground, in various directions (vertical, horizontal) [22,25–27], and also in microgravity either in sounding rockets or on board of parabolic flights [12–14,28].

In the framework of the European Space Agency (ESA) project entitled XRMON (*In situ* X-ray monitoring of advanced metallurgical processes under micro gravity and terrestrial conditions), an *in situ* investigation of the columnar solidification in a non-refined Al–20wt.%Cu alloy was conducted for the first time in microgravity, on board the MASER-12 sounding rocket [13]. This study provided direct comparison of terrestrial and microgravity alloy solidification. In the subsequent stage of the project, the first *in situ* study in microgravity of equiaxed solidification in isothermal conditions was performed in the MASER-13 sounding rocket [29] with a refined Al–20wt.%Cu alloy [14]. In the continuation of those investigations, the present work presents the first microgravity experiment dedicated to the *in situ* observation of the Columnar-to-Equiaxed Transition in a refined Al–20wt.%Cu alloy. The experiment was conducted in the XRMON-GF2 (Gradient Furnace) facility on board of the MASER-14 sounding rocket. To complement this microgravity experiment, three ground reference experiments in horizontal, vertical upward and vertical downward configurations were

performed with nearly the same control parameters. A comparative analysis has been conducted between the microgravity experiment in diffusive conditions and the ground-based experiments to enlighten gravity effects during the different steps of the CET. Details of the experimental configuration and the experiment timeline will be presented in the first part of this document. In the second part, the columnar growth, CET and equiaxed regime will be depicted. In the last part, discussions on the equiaxed grain nucleation step prior to CET, the blocking mechanisms responsible for CET and the final equiaxed grain structures will be presented.

2. Experiment description

2.1. MASER-14 sounding rocket

The MASER-14 (MAterials Science Experiment Rocket) sounding rocket is a sub-orbital vehicle developed by the Swedish Space Corporation (SSC) to perform experiments during short-duration microgravity flights. It was launched on June 25th, 2019 at the Esrange Space Centre in northern Sweden. The 400 kg scientific payload was composed of 4 experimental modules including the XRMON-GF2 experiment (Fig. 1a). The rocket followed a parabolic trajectory from launch to landing with an apogee of 245 km, providing approximately 6 minutes of microgravity.

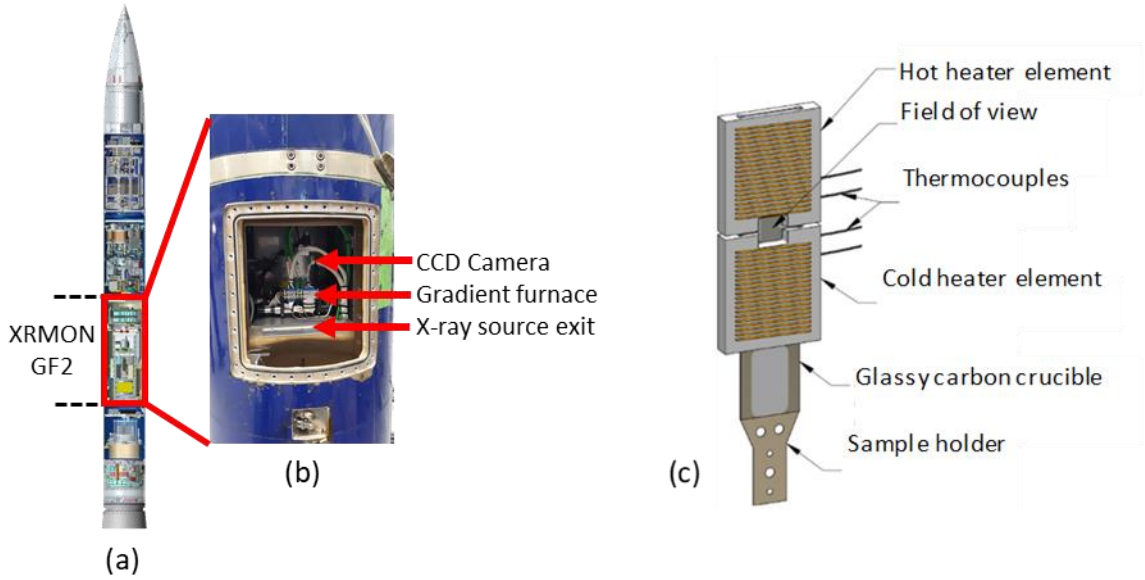

Fig.1: (a) Scheme of the payload of the rocket with the XRMON-GF2 module located near the bottom of the payload, (b) photograph showing the XRMON-GF2 facility installed inside the module and (c) schematic layout of the XRMON-GF2 furnace (courtesy of A.G. Murphy, UCD)

2.2. XRMON-GF2 facility

The XRMON-GF2 facility is a duplicate of the XRMON-GF (Gradient Furnace) facility developed for the MASER-12 sounding rocket experiment [13] in the framework of ESA XRMON project dedicated to the application of X-radiography during microgravity experiments. It is also similar to XRMON-PFF (Parabolic Flight Facility), which was used during parabolic flights experiments [12] and the SFINX (Solidification Furnace with IN Situ X-radiography) laboratory device [29]. A complete description of those facilities has been presented in these papers. Only a short summary of the main features will be given below.

The XRMON-GF2 facility consists mainly of a Bridgman-type gradient furnace and an X-radiography system. The solidification furnace consists of two heaters separated by an adiabatic

gap. The adiabatic gap separating the heating elements contains a 5 mm × 5 mm window in its centre that constitutes the Field of View (FoV) through which the X-rays pass, thus allowing an *in situ* and real-time analysis of the solidification experiments. The two heaters impose a longitudinal temperature gradient G_{app} controlled by two K-type thermocouples spaced 15 mm apart: one placed in the hot zone 5 mm from the top of the field of view, the other one in the cold zone 5 mm from the bottom of field of view. The gradient furnace enables directional solidification with applied temperature gradient within the range of 5–15 °C/mm and controlled cooling rates within the range of 0.01–1.5 °C/s.

The X-radiography system consists of a micro-focus X-ray source with a molybdenum target (3 µm focal spot) delivering a photon flux with two peaks of energy 17.4 keV and 19.6 keV, ensuring a good contrast to study Al–Cu based alloys. The detector system comprises a scintillator plate and a CCD digital camera with a pixel size of 20 µm. The microfocus source delivers a conical beam leading to a magnification of the image depending on the respective distance between the source, the sample, and the camera. For the current geometry, the magnification is about 5 and the effective pixel size at the level of the sample is 4 µm.

The four foil-like samples investigated were Al–20wt.%Cu alloys with grain refiner (0.1 wt% Al–Ti–B) that were 50 mm in length, 5 mm in width, ~210 µm in thickness and 3 µm finish-polished. The thickness value is a good compromise between having a good radiographic contrast, reducing convection effects, and avoiding the superimposing of several layers of dendrites, which would be detrimental to the picture legibility. The samples were sandwiched

between two flexible glassy carbon sheets sewn together with a silica thread, whilst held in place in the middle of stainless-steel spacers. The holder/crucible/sample was then slid into the furnace and straddled both heater elements to achieve the expected thermal profile.

Al–20wt.%Cu alloy with grain refiner was chosen to be consistent with the MASER-12 experiment where the same alloy, in non-refined form, was used to study columnar solidification, and the MASER-13 experiment where the same alloy, also grain-refined, was used to study equiaxed solidification. The contrast in radiography between the alpha-Al grains and the Cu rich-solute is high for this alloy composition, ensuring a better visualisation of the microstructure. Moreover, solid aluminium is lighter than liquid Al–20wt.%Cu, which enhances buoyancy effects during vertical solidification experiments by pushing the aluminium grains upward. Also, for downward solidification experiments, both thermal and solutal gradients are destabilizing and strong convective flows are expected.

2.3. Microgravity experiment parameters

A well-adapted experimental timeline has been defined based on ground-based tests to ensure that both the melting and the cooling stages would be achieved within the short microgravity period of roughly six minutes. The chosen timeline is shown in Fig. 2 where $t_0 =$ 0 s corresponds to the sounding rocket lift-off time. The sample was pre-heated before lift-off at a rate of 2 °C/s from 20 °C to 540 °C, which is below the eutectic temperature $T_E = 548.2$ °C to keep the sample fully solid. The sample melting phase started 14 s before the beginning of

the microgravity period by increasing the temperature of both heaters at a heating rate of 2 °C/s until reaching the target temperatures. The melting phase ended at t = 150 s, when the "cold" heater reached 572 °C and the "hot" heater reached 722 °C, which is above the alloy liquidus temperature T_L = 605 °C and corresponds to an applied temperature gradient G_{app} = 10 °C/mm. At the end of the melting phase, the sample was partially melted, and some solid phase remained in the relatively cold part of the field of view, constituting the initial solid-liquid interface.

The solidification was triggered at t_{R1} = 165 s by applying the first cooling rate R_1 = 0.08 °C/s to both heaters. This value was chosen from ground-based tests to obtain a columnar solidification front. A second cooling rate R_2 = 1 °C/s was applied on both heaters at t_{R2} = 390 s to provoke the columnar-to-equiaxed transition. Finally, the two heaters were switched off at the end of the microgravity period and the sample cooled down naturally.

During the whole experiment, uncompressed images were recorded and stored on board at a frame rate of 3 images per second, which was sufficient to follow the microstructure development. Image processing was enabled on board to improve the radiograph quality by a flat-field correction. In this method, the solidification images were divided by a reference image recorded at the end of the melting phase [30].

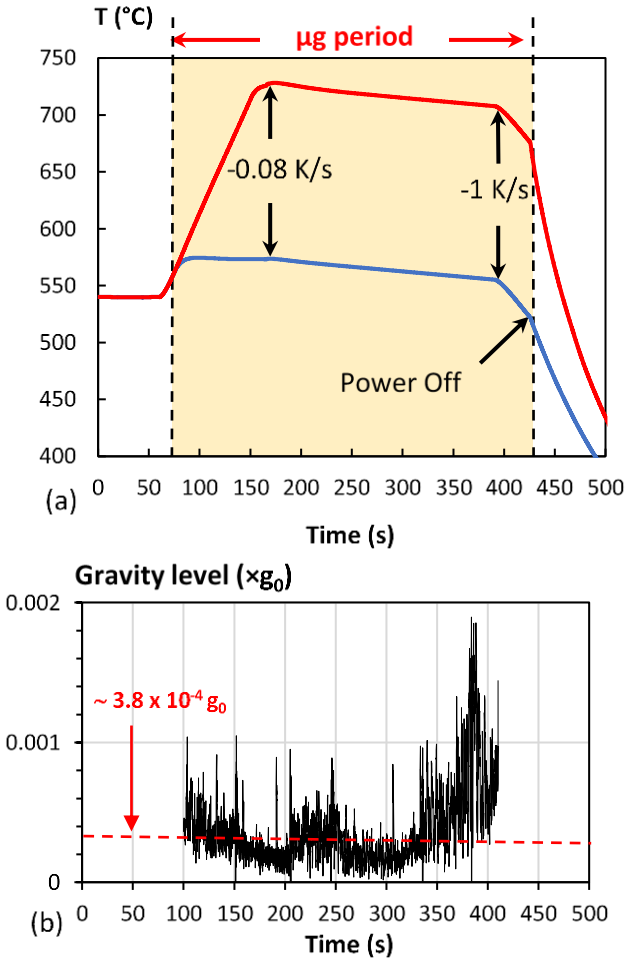

Fig. 2. (a) MASER-14 flight timeline (Time t_0=0 s corresponds to the lift-off time) and (b) gravity level with time during the µg period (the red dashed line corresponds to the average gravity level value)

2.4. Ground-based experiment parameters

For a sake of comparison, three experiments were performed on Earth using the same XRMON-GF2 furnace, the same cooling rates R_1 and R_2 and applied temperature gradient G_{app} but with different solidification configurations (horizontal, upward, and downward solidifications). A fresh refined Al–20wt.%Cu sample was used for each experiment.

- Horizontal solidification, with the main surface of the sample set perpendicular to the gravity vector. In this configuration, gravity effects are expected to be minimized significantly [31].
- Vertical upward solidification (counter-gravity direction). In this configuration, both thermal and solutal gradient are stabilising but buoyancy will induce the flotation of unconstrained solid grains [21].
- Vertical downward solidification (in-gravity direction). In this configuration, both thermal and solutal gradients are destabilising and strong convective flow is expected [22].

It is worth noting that for both vertical solidification experiments, grain flotation and convective flow dramatically affected the melting of the sample. Consequently, the timelines of melting phase of both vertical experiments were slightly adapted to better control the initial position of the solid-liquid interface. More precisely, the temperature gradient G_{app} was applied after the two heaters reached a temperature of 300 °C and a slower heating rate of 0.5 °C/s was imposed to the heating elements during the melting phase.

2.5. Grain structure characterisation

The solidification process was observed *in situ* by using X-radiography. The solidification sequence consisted of the growth of a columnar front followed by an equiaxed front propagating from the cold zone towards the hot zone of the FoV. A quantitative analysis was made to determine the grain size and grain elongation distribution of the equiaxed microstructure. The procedure was described in detail in [22,29] and only the main steps are summarised hereafter.

Based on the radiographs recorded during the solidification process, the contouring of the grains was performed manually using the free software ImageJ [32]. Then, using a semi-automatic macro script, it was possible to determine two characteristic grain features: the grain size, defined as the diameter d of a disk having the same surface area, also called the equivalent disk. This parameter gives no information about the grain morphology and was complemented by the grain elongation factor ϕ, defined as $\phi = L_1/L_2$ with L_1 the length of the longest straight segment inscribed within the grain (main axis), and L_2 the length of the longest straight segment inscribed within the grain and orthogonal to the segment that gives L_1. This factor varies from unity for a fully equiaxed grain to larger values for elongated grains.

3. Experimental observations

3.1. Microstructure formation during columnar growth

The objective of the present study was to experimentally investigate the Columnar-to-Equiaxed Transition in a refined Al–20wt.%Cu alloy in microgravity conditions, and on ground with different orientations of the sample with respect to the gravity vector. A series of radiographs recorded during the solidification of the samples is shown in Fig.3 for these four experiments: solidification in microgravity, horizontal solidification, vertical upward solidification, and vertical downward solidification.

Four radiographs were selected for each configuration to show the formation of the microstructure in the FoV. Complete solidification sequences are available online

(supplementary movies 1, 2, 3 and 4). As mentioned in section 2.3, the samples were first partially melted. An initial solid-liquid interface was required to start the columnar solidification from already present solid parts and thus prevent the occurrence of a high undercooling in the liquid that would have triggered the nucleation of many grains on the refining particles. The columnar growth started with the application of the low cooling rate R_1 = 0.08 °C/s and dendrites progressively developed from the solid parts of the initial solid-liquid interface (Fig.3a and Fig.3b). A dark layer is visible ahead of the solidification front due to the rejection of Cu during solidification as previously reported in synchrotron experiments [30], and during the MASER-12 sounding rocket campaign [13]. It is worth mentioning that Cu-rejection during the downward solidification experiment led to the development of solute plumes, corresponding to a downward flow of Cu-rich liquid (Fig.3b3 and supplementary movie 4) because the rejected solute (Cu) is denser than the solvent (Al). The solute plumes impacted the growth of some columnar dendrites by locally increasing the Cu concentration ahead of the dendrite tip and thus retarding their growth. Similar observations have been reported in detail in previous studies [22,26,33,34].

Vertical lines and white areas are visible on the right-hand and left-hand sides of the microgravity and horizontal samples. These features are attributed to sample deformation due to solidification-induced shrinkage flow as well as bubble formation and collapse, which induces a local change of the thickness and therefore of the X-ray transmission. The fact that the changes in thickness appear with a high contrast is due to the contrast enhancement of the

images that was applied to better distinguish the solid and the liquid phases. Post-mortem measurements showed that the sample was about 10 µm thicker in the centre after solidification. It is assumed that these deformations did not significantly disturb the propagation of the solidification front. Such deformations were not observed in the two vertical configurations because the hydrostatic pressure of the liquid on the crucible wall maintained the sample shape after the melting step. The use of a more rigid crucible might help reduce sample deformation in future experiments.

In addition to the development of columnar dendrites, some elongated grains are also visible (white circles in Fig.3a and Fig.3b). The observations show that these grains nucleated ahead of the columnar front for the microgravity, horizontal and downward solidification experiments, probably on refiners, impurities, or heterogeneities of the oxide layer. Those grains slightly moved towards the cold part of the sample during their development. In the case of the microgravity and horizontal experiments, this motion can be attributed to advective flow induced by solidification shrinkage as already reported for experiments carried out in similar configurations [21,22,31]. In the case of the downward solidification experiment, the grain motion is due to buoyancy since the Al-rich solid parts are less dense than the surrounding liquid. The origin of the grains was different for the upward solidification experiment. Close inspection of the radiograph sequence revealed that no grain nucleation occurred, but copious columnar dendrite fragmentation happened. The fragments floated due to buoyancy and moved toward the hot part of the sample where they gradually melted. The grains visible in Fig. 3a2

and Fig. 3b2 (dashed white circles) are in fact fragments that remained stuck in the sample thickness while floating. Such differences between the various experiments could not have been deduced from post-mortem analyses, which highlight the interest of *in situ* observations [35]. It is worth mentioning that all fragments would float and melt for experiments carried out in bulk samples, leading to a different final grain structure. This might not always be the case as shown by Zimmermann *et al.* [35] on non-refined Al-10wt.%Cu alloys for which the solid and liquid density are close. In the latter study, experiments in 3D bulk samples and in 2D sheet-like samples produced the same results with respect to the fragmentation process and the resulting grain structure.

As previously mentioned, the formation of gas bubbles due to the presence of residual hydrogen gas was noticed. Bubbles that nucleated in the liquid melt grew and eventually collapsed, leaving circular-shape deformations. Bubbles that nucleated in the mushy zone caused small displacement of the dendrites while developing and left spherical liquid areas after collapsing. Similar behaviors have been recently reported and studied in details for instance by Murphy *et al.* [36] and Werner *et al.* [37]. In vertical configuration, the bubbles floated due to buoyancy and/or thermal Marangoni effect [38]. In microgravity conditions, the bubbles moved toward the hot part of the sample only due to thermal Marangoni convection because the applied temperature gradient was sufficient to cause a significant variation of the surface tension at the gas-liquid interface. Surface flow occurred in the direction of increasing tension, causing the gas bubbles to move in the direction of increasing temperature. A similar behavior was not

observed in the horizontal configuration although the same temperature gradient was applied, because the bubbles were stuck on the upper wall of the sample thickness due to buoyancy. Here, Marangoni convection was not strong enough to induce bubble motion. For the upward and downward experiments, only few bubbles occurred during the solidification step. This is likely due to the longer time that was taken to position the solid-liquid interface. Bubbles formed and collapsed during this adjustment period and most of the gas was released when the solidification experiments started. A thorough investigation of the bubble behaviour is out of the scope of the present study and is expected to be the subject of future studies. Besides, the impact of gas bubbles on columnar growth and CET was poor for the present experiments.

3.2. CET and equiaxed front propagation

After the formation of columnar structures, the cooling rate was sharply increased from R_1 = -0.08 °C/s to R_2 = -1 °C/s to trigger a Columnar-to-Equiaxed Transition (CET). The CET occurred in three steps. Firstly, the nucleation of many equiaxed grains occurred ahead of the columnar front due to an increase of the constitutional undercooling in front of the dendrite tips. Refiners present in the alloy were activated and a great number of nucleation events occurred, in accordance with the free growth model proposed by Greer et al. [39]. The new grains appeared as a layer of small equiaxed dendrites ahead of the columnar front (Fig. 3c). The images in Fig 3.c and 3.d were divided by the last image recorded before application of the second cooling rate to remove contrasts due to sample deformation, which was helpful to

distinguish more clearly the new grains and reveal the amount of solidified columnar dendrites after initiating the second cooling rate. The first layer of grains appeared in approximately 6 to 7 seconds after application of the second cooling rate for the microgravity experiment, slightly earlier than in the upward (8 s) and horizontal (9 s) configurations. Almost twice the time was necessary to form the first layer of grains for the downward configuration (11 s to 12 s). In addition, the new grains seemed to nucleate slightly farther from the columnar front in the case of the microgravity experiment. This observation will be discussed in more detail with the help of quantitative measurements in section 4.1.

Secondly, the growth of the columnar grains was blocked by the development of the new equiaxed grains. The number of new grains was sufficient in each experimental configuration to block the growth of the columnar dendrites and induce a sharp CET. Two blocking mechanisms were observed: mechanical (hard) blocking when the equiaxed grains and columnar dendrites came into direct contact, and solutal (soft) blocking when the accumulation of solute in the interdendritic region led to the arrest of the columnar growth. The relative importance of those two mechanisms on the blocking of the columnar front will also be discussed in more detail in section 4.2.

Finally, the growth of the columnar front is replaced by the propagation of an equiaxed effective front. The newly nucleated grains develop in the temperature gradient direction and a constitutionally undercooled liquid zone progressively forms ahead of the dendrite tips due to solute rejection. Under these circumstances, a new layer of grains can only nucleate once the

liquid undercooling reaches the nucleation undercooling of the refining particles. Thus, the nucleation phases are separated by no-nucleation periods during which grain growth occurs and the equiaxed effective front propagates in a wave-like type as reported by many authors [40–43]. The last images recorded during the experiments are shown in Fig.3d. They show that both the equiaxed effective front and the grain structure are similar for all the solidification configurations. This suggests that gravity did not impact much the solidification process at this cooling rate (R_2 = -1 °C/s). This point will be investigated in more detail in section 4.3.

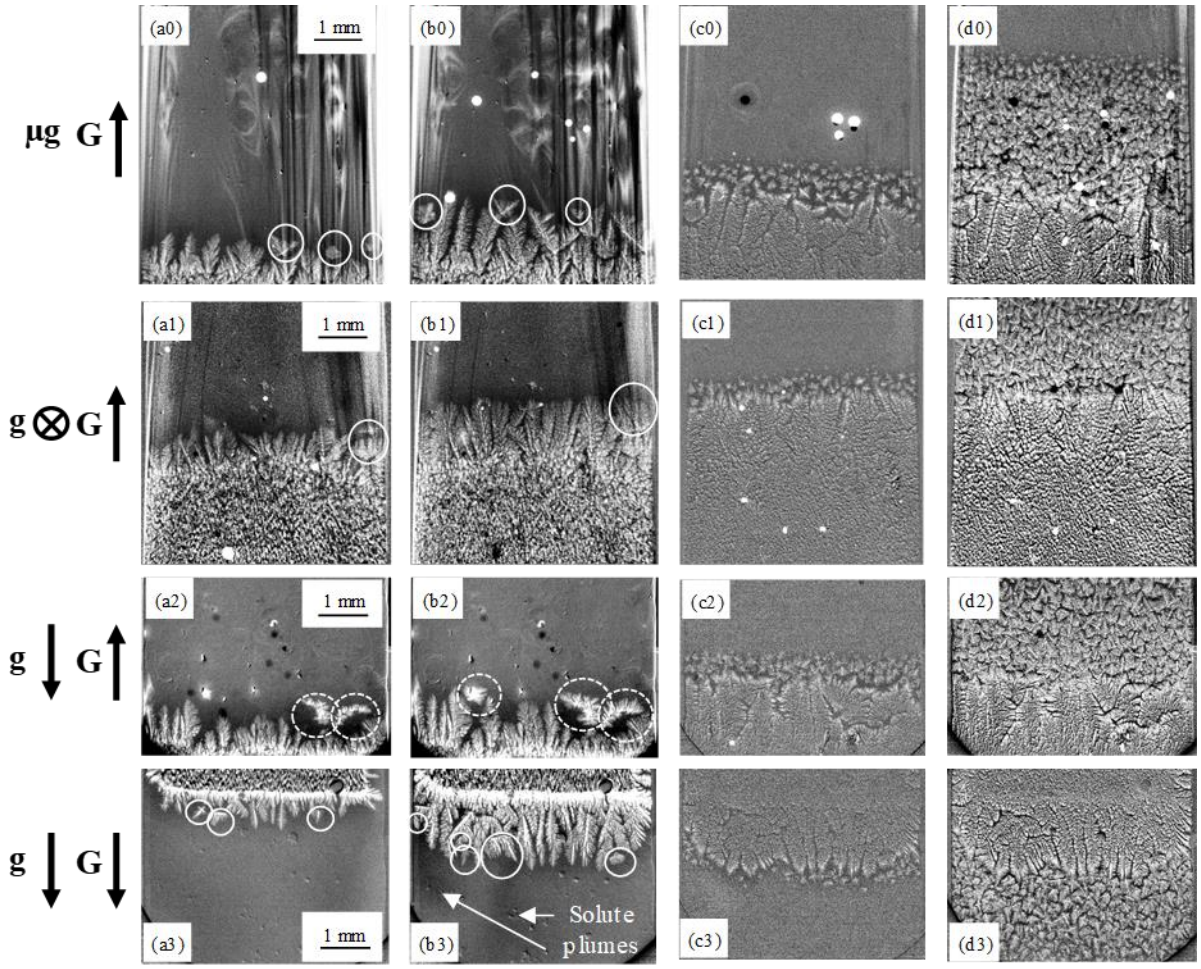

Fig.3: Radiographs of the whole solidification sequence. From top to bottom: microgravity experiment, horizontal configuration, upward configuration, and downward configuration. (a) Beginning of the columnar growth for the cooling rate R_1 = 0.08 °C/s, (b) solidification front before application of the second cooling rate R_2 = 1 °C/s, (c) nucleation of new grains (images were taken 11 s after application of R_2) and (d) final grain structure. Images in (c) and (d) were divided by the last image recorded before applying the cooling rate R_2 to better visualise the newly nucleated grains.

3.3. Growth rate measurements

The time evolution of the solidification interface position in the field of view y_{int} can be determined based on the radiographs. The results of these measurements are shown in Fig. 4 for the four experimental configurations. During the columnar regime, the measured positions

correspond to the highest dendrite tip of the columnar grain network (black circles in Fig. 4). During the equiaxed regime, the measured positions correspond to the highest dendrite tip of the equiaxed grain network forming the effective equiaxed front (red diamonds in Fig. 4).

After application of the first cooling rate (R_1 = –0.08 °C/s) the columnar interface moves slowly toward the hot end of the field of view then gradually accelerates to eventually reach a quasi-linear regime. The corresponding growth rate V_{Col} was deduced by fitting the data to a linear law (black lines in Fig. 4). The effective equiaxed front growth rate V_{Eq} was also measured by using the same procedure after initiating the second cooling rate (R_2 = –1 °C/s). The measured velocities are summarised in Table 1. The systematic error on the velocity values was deduced from the error on the position measurement (± 4 µm) that depends on the pixel size. For the columnar regime, growth velocities are in the same order of magnitude within the error bars, which indicates that the four configurations are comparable. For the equiaxed regime, the growth velocities are also in the same order of magnitude except in the case of the downward configuration where the growth velocity is slower. This is likely because the whole experimental system could not be rotated upside-down to obtain a temperature gradient parallel to gravity. Instead, the system remained with the same orientation and the temperature values of the heaters were swapped (the “hot” heating element became the “cold” heating element, and the “cold” heating element became the “hot” heating element). Then, because of the asymmetry of the sample holder design as visible in Fig.1c, a different heat extraction and thermal field can have induced slower growth.

The actual temperature gradient in the sample could be estimated by using the relation $G = R.V$, with V the velocity of the solidification front. The temperature gradient values are summarised in Table 1. It is worth noting that the measurements show that the actual temperature gradient inside the sample was slightly different from the applied temperature gradient G_{app} = 10 °C/mm. The discrepancy can be attributed to the difference in thermal diffusivity between the sample, the crucible, and the furnace. Further numerical simulations of the experimental device need to be considered to get a better understanding of the temperature field evolution and will be the subject of future investigations.

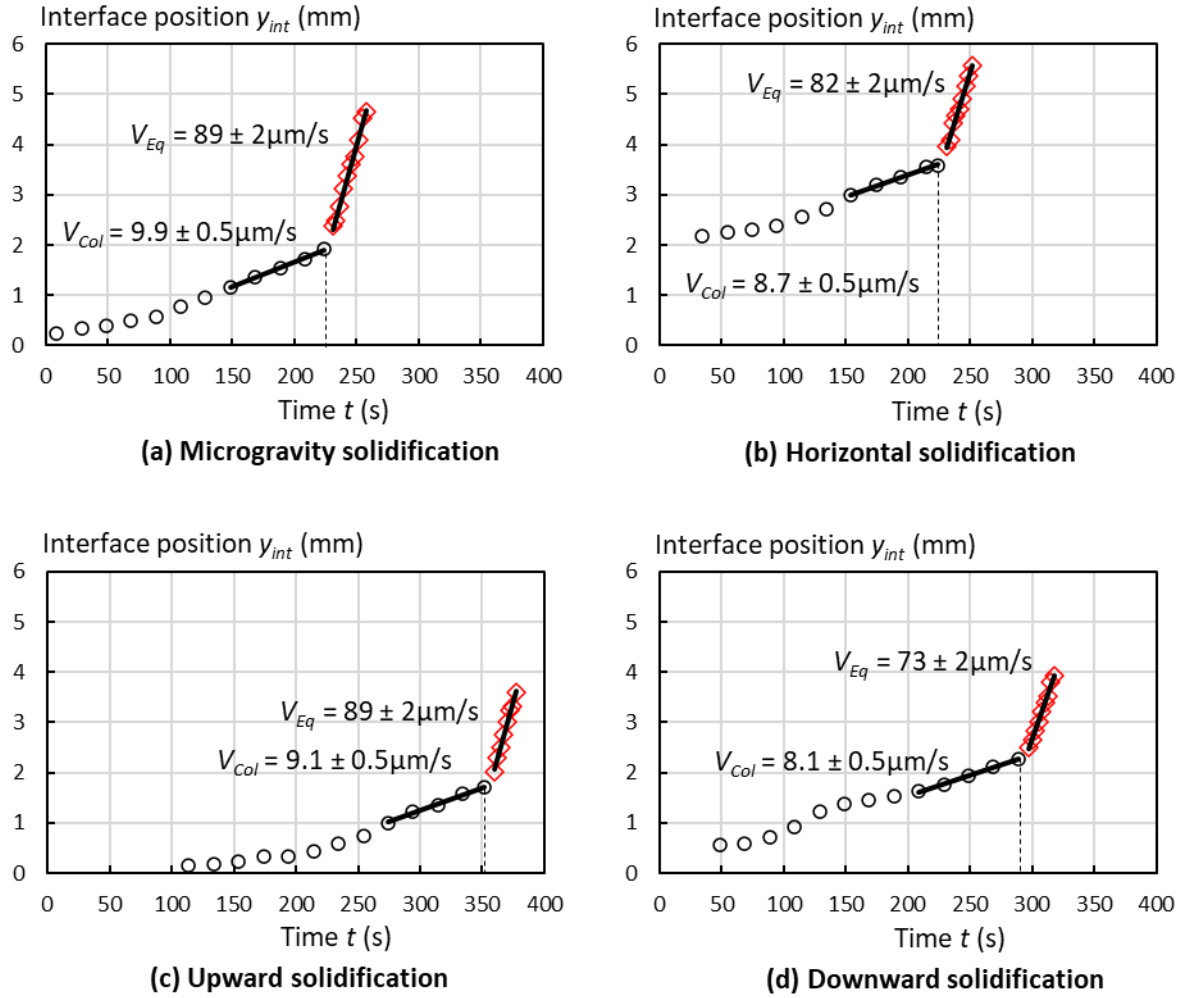

Fig. 4: Measurement of the solidification interface position y_{int} in the field of view as a function of time (columnar regime in black circles, equiaxed regime in red diamonds, color available online): (a) microgravity, (b) horizontal, (c) upward and (d) downward experiment. The reference time (t = 0 s) is taken at the application of the first cooling rate. The vertical dashed line in each plot indicates the time of the cooling rate increase from R_1 = –0.08 °C/s to R_2 = –1 °C/s. The columnar (resp. equiaxed) interface growth rate V_{Col} (resp. V_{Eq}) was deduced by fitting the data to a linear law (thick black lines).

	Microgravity	Horizontal	Upward	Downward
V_{Col} (µm/s)	9.9 ± 0.5	8.7 ± 0.5	9.1 ± 0.5	8.1 ± 0.5
G_{Col} (°C/mm)	8.1 ± 0.4	9.2 ± 0.5	8.8 ± 0.5	9.8 ± 0.6

V_{Eq} (µm/s)	89 ± 2	82 ± 2	89 ± 2	73 ± 2
G_{Eq} (°C/mm)	11.2 ± 0.2	12.2 ± 0.3	11.2 ± 0.2	13.7 ± 0.4

Table 1: Measured solid-liquid interface velocities and estimated temperature gradients for the four experiments.

4. Discussion

The comparison between ground and microgravity experiments is an effective approach to reveal the impact of convection and buoyancy on solidification microstructure formation as demonstrated for instance by Dupouy *et al.* [44], Nguyen-thi *et al.* [13] or Murphy *et al.* [31]. It is also an essential step to obtain benchmark data for comparisons with theoretical models and numerical simulations. The impact of gravity on the CET for these different configurations will be discussed in the following parts.

4.1. Nucleation step

As mentioned in section 3.2, the first layer of equiaxed grains appeared later in the downward case upon initiating the second cooling rate (Fig. 3c). This indicates that a longer time was necessary to increase the constitutional undercooling ahead of the solidification front and induce grain nucleation. To investigate the origin of this feature, the temperature data were checked, which showed that this difference was not due to a heater regulation issue. A different composition profile ahead of the columnar front can be a possible origin for the different undercooling distribution in the liquid. In radiograph images, the gray level values in the liquid

phase are qualitatively related to the solute concentration: the lower the gray level, the higher the solute concentration. Fig.5 shows gray level profiles measured for the four solidification configurations in front of the highest dendrite tip of the columnar grain network and just before initiating the second cooling rate. A moving average was calculated (red line in Fig.5) to smooth out fluctuations due to noise in the images. A solute layer is clearly visible for the microgravity, horizontal and upward experiments (Fig.5a to Fig.5c). It was also detected for other dendrites of the columnar fronts. The extension of the solute layers are of the same order of magnitude as the characteristic diffusive solutal length $l_s = D_s/V \approx 333$ µm, with $D_s = 3 \times 10^{-9}$ m²/s the solute diffusion coefficient [45] and $V = 9$ µm/s the average growth velocity. In stark contrast to those experiments, no solute layer was visible ahead of the dendrite tip in the downward experiment with the current spatial resolution. Instead, a constant gray value was obtained and only very short solute layers, often difficult to distinguish, were observed for other dendrites. This difference in solute boundary layer is ascribed to thermo-solutal convective flow that was most likely strong enough to sweep away the solute rejected during solidification [22]. Consequently, additional time after initiating the second cooling rate was necessary to build up a solutal layer with a sufficiently constitutionally undercooled zone where equiaxed grains could nucleate like in the other experimental configurations.

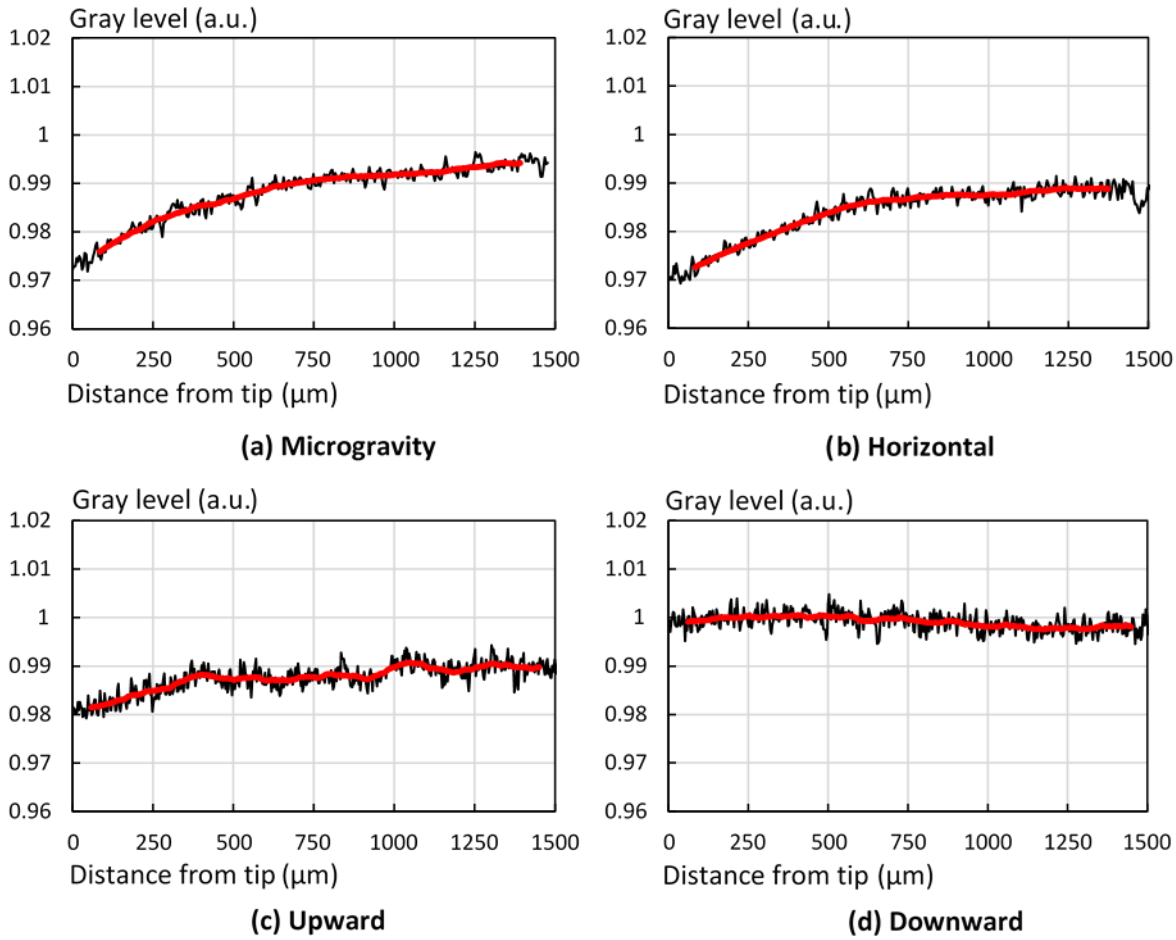

Fig. 5: Gray level variation ahead of the highest dendrite tip for the four experimental configurations. The red curves correspond to the moving average.

Interestingly, the solute profile ahead of the columnar front only slightly changed when the first equiaxed grains appeared as illustrated in Fig. 6a for the microgravity experiment. The two curves show the gray level variation in front of the highest columnar dendrite when the second cooling rate was applied at $t = t_{R2}$ (black curve), and later at $t = t_{R2} + 7$s (red curve). The two peaks in the red curve correspond to two equiaxed grains that nucleated in front of the dendrite tip. Indeed, the X-ray absorption of the Al-rich solid grains is lower than the Cu-rich liquid,

therefore they appear with a higher gray level. The equiaxed grains nucleated even though the concentration profile did not substantially change. This suggests that a change in concentration profile was not the main cause of the constitutional undercooling increase in the liquid, which is necessary to activate the refiners. Given that the Lewis number, defined as the ratio between the thermal diffusivity D_T and the solutal diffusivity D_S is large ($Le = D_T / D_S = 2.17 \times 10^4$ with $D_T = 6.5 \times 10^{-5}$ m²/s [46] and $D_S = 3.5 \times 10^{-9}$ m²/s), the sample temperature rapidly decreased after the abrupt change of the cooling rate. Meanwhile, the concentration profile did not have time to significantly evolve (Fig.6b and Fig.6c). Consequently, the increase of the constitutional undercooling $\Delta T = T_{eq} - T_L$ (with T_{eq} the local liquidus temperature deduced from the phase diagram and T_L the temperature of the liquid imposed by the temperature gradient) can be attributed to the rapid decrease of the temperature as illustrated in Fig.6c.

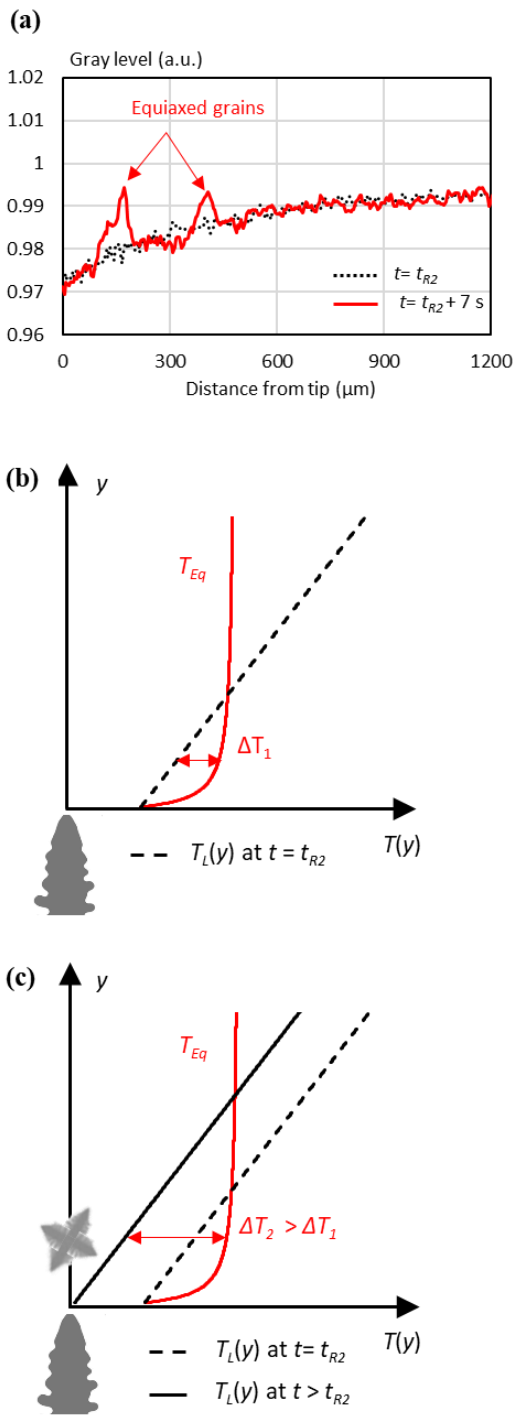

Fig.6: (a) Gray level variation ahead of the highest columnar dendrite tip (microgravity case). The black curve is the gray level measured at $t = t_{R2}$ and the red curve is the gray level measured at $t = t_{R2} + 7s$. The two peaks in the red curve corresponds to equiaxed grains that nucleated in front of the dendrite. (b) Graph illustrating the constitutional undercooling intensity ahead of a columnar dendrite at $t = t_{R2}$ and (c) the increase of the constitutional undercooling intensity after the rapid change in cooling rate at $t > t_{R2}$.

Another difference related to grain nucleation was also observed between the experiments. As mentioned in section 3.2, it seems that the grains nucleated farther from the columnar front in the microgravity case. Complementary measurements were made to quantitatively analyse the distance at which the equiaxed grains nucleated from the columnar dendrites. This nucleation distance d_n was defined as the distance between the centre of the newly nucleated grains and the nearest columnar dendrite tip as illustrated in Fig.7. This measurement was performed for the first layer of equiaxed grains, which corresponds to approximately 30 grains, and for all solidification configurations (it is worth noting that the number of grains of the first layer are very close for the four experiments). The results are shown in Fig.8.

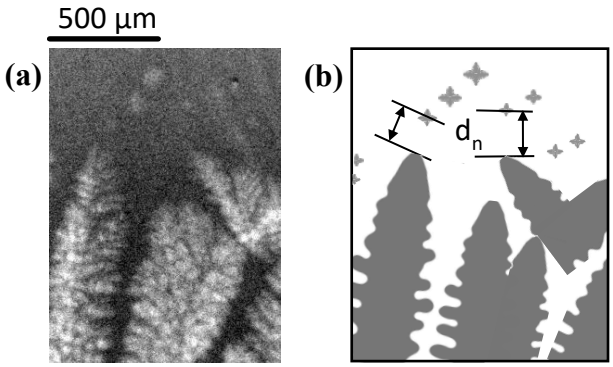

Fig.7: (a) Radiograph showing columnar dendrites with newly nucleated equiaxed grains ahead and (b) sketch showing the nucleation distance d_n between the centre of an equiaxed grain that nucleated ahead of the columnar front and the nearest columnar dendrite tip.

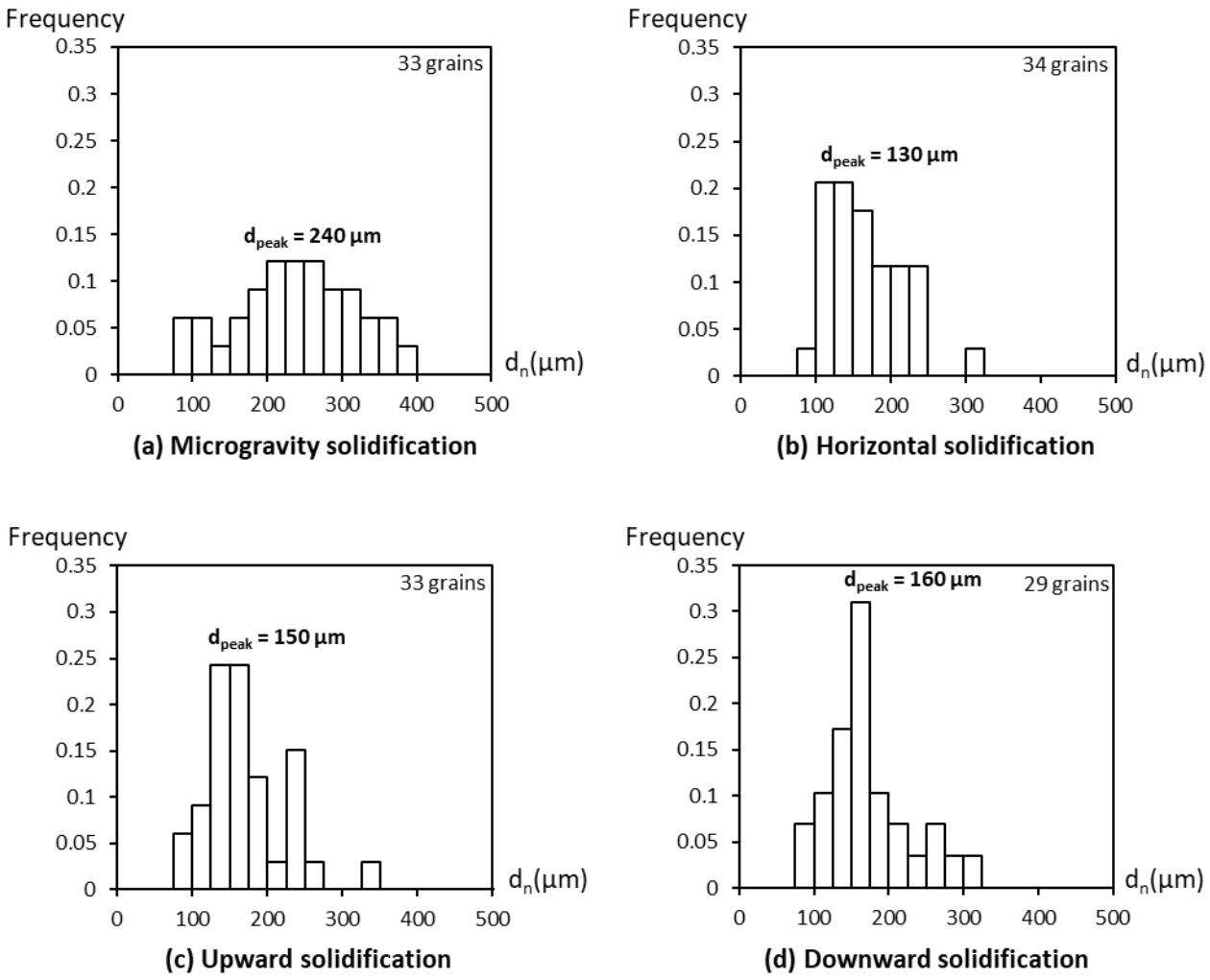

Fig.8: Distribution of the nucleation distance. (a) Microgravity experiment, (b) horizontal configuration, (c) upward configuration and (d) downward configuration.

For every experiment, a distribution of the nucleation distance was obtained within a range of 75 µm to 400 µm. This can be attributed to the fact that there exists a distribution of the refining particle size. According to the free growth model proposed by Greer [39], particles with small diameters require a higher undercooling intensity than particles with a large diameter for grain nucleation to occur. Thus, grains that nucleate on particles with a large diameter will

appear far from the columnar dendrites, where the constitutional undercooling is lower. In the same way, grains that nucleate on particles with a small diameter will appear closer to the columnar dendrites, where the constitutional undercooling is higher.

In addition, clear differences can be noticed between the four graphs. The measurements confirm that the equiaxed grains appeared farther from the columnar front for the microgravity experiment, at around 240 µm from the columnar dendrite tips, which was much larger than the values of around 150 µm for the ground experiments. These discrepancies suggest that gravity and convective flow had a significant impact on the grain nucleation process. It is well known that convective flows on Earth can induce a narrower solute layer compared to the purely diffusive case in microgravity. Models based on the concept that solute transport is assumed diffusive inside a boundary layer (also referred as stagnant film) and that the solute is completely homogenised due to convection outside of the boundary layer have been successful to mimic the effect of convective flow on solidification [47,48]. Thus, the closer distance at which equiaxed grains appeared for the ground experiments can be attributed to convective flow that shortens the solute layer ahead of the columnar front and reduces the extent of the undercooled zone where grains can nucleate. The gray-level profiles reported Fig.5 show that the solute layer before increase of the cooling rate is shorter for the upward and downward solidification experiments. This is less obvious for the horizontal solidification that has a solute profile comparable to the microgravity experiment but for which the equiaxed grains nucleated the closest to the columnar front. The origin of the latter discrepancy is not clear. As for

downward solidification, the horizontal configuration is both thermally and solutally unstable with respect to convective flow [47]. Thus, the concentration pile-up, and therefore the concentration profile, could be modified in a way that the maximum of constitutional undercooling would be closer to the solidification front than in microgravity. Experiments with better spatial and temporal resolution would be necessary to carry out a more accurate analysis of the modification of the solute profile during the transient stage following the application of the second cooling rate. Another phenomenon that cannot be characterised currently with the present experimental observation technique is the impact of buoyancy and convective flow on the refining particle distribution, which could also modify the position at which the first grains would nucleate. Advanced numerical simulation that would account for both dendrite growth and convective flow would be helpful to improve the understanding of the present experimental observations.

4.2. Blocking of the columnar dendrites

The CET was triggered by initiating the second cooling rate R_2 = -1 °C/s which was significantly faster than R_1 = -0.08 °C/s. As discussed in the previous section, this rapid change of the cooling rate induced an increase of the constitutional undercooling in the liquid ahead of the columnar dendrites, which led to the refiner activation and numerous equiaxed grain-nucleation events. The high number of new grains was sufficient in each experimental configuration to eventually lead to the blocking of the columnar dendrites and induce a sharp

CET.

The two blocking mechanisms reported in the literature were observed. During mechanical (hard) blocking [2], the equiaxed grains came in direct contact with the columnar dendrites as illustrated in Fig. 9a. During solutal (soft) blocking [3], there was no contact and the growth of the equiaxed and columnar grains was progressively stopped due to the accumulation of solute in the interdendritic region as illustrated in Fig. 9b. Solute accumulation between the dendrites induced a smooth increase in the far-field concentration with concomitant decrease in the solute gradient that drives the growth rate, as reported by Bogno *et al.* [45] and Becker *et al.* [49] in the case of isothermal experiments.

Additional measurements were made to quantitatively determine the relative importance of each mechanism on the blocking of the solidification front. The measurements were made on the most advanced dendrites of the columnar front and the results are reported in Fig. 9c. It shows that the main blocking mechanism for the microgravity and horizontal experiments was mechanical blocking. This may seem surprising since equiaxed grains could be expected to be fixed in the absence of gravity, as well as in horizontal configuration when grain motion due to buoyancy is limited to the small thickness of the sample. However, the drag flow induced by solidification shrinkage can be significant during solidification experiments as studied by Vernède *et al.* [50] and reported by Salloum-Abou-Jaoude *et al.* [21]. Drag flow induced by solidification shrinkage is a non-gravity-related effect and was at the origin of equiaxed grain motion toward the columnar front. The motion of 15 representative equiaxed grains has been

investigated. The average velocity was 20 µm/s and varied between 10 and 30 µm/s depending on the interaction with the neighbouring grains. Grain motion was observed as soon as the grains were visible, and most dendrites were consequently mechanically blocked.

For the two vertical experiments, both mechanical and solutal blocking mechanisms were observed in more similar proportions. On one hand, like in the microgravity and horizontal experiments, solidification shrinkage was at the origin of grain motion toward the cold part of the sample, which induced mechanical blocking. On the other hand, grain motion was also due to buoyancy force in the case of the vertical configuration. The origin of solutal blocking is different for the upward and downward solidification experiments. The image sequence shows that during upward growth, the equiaxed grains did not move toward the cold part as soon as visible as in the microgravity and horizontal experiments. This delay is probably due to a competition between shrinkage flow and buoyancy. For some grains, the shrinkage flow is strong enough to overcome the buoyancy force and mechanical blocking occurs. For other grains, the balance between shrinkage flow and buoyancy leaves time to grains to form a coherent network preventing them from moving and thus promoting columnar dendrite blocking through solutal interaction. In the downward case, the grains moved toward the cold top part of the sample under the sum of both shrinkage flow and buoyancy. In some regions, the grains piled up to form bridges ahead of columnar dendrites, which lead to the solutal blocking of the latter.

The present observations and measurements show that both mechanical and solutal

1 blocking mechanisms come into play to induce CET. This highlights the fact that models
2 describing both grain packing, as recently investigated both experimentally and numerically by
3 Olmedilla *et al.* [51], and solutal interactions, as studied for instance by Boukellal *et al.* [52]
4 using a phase-field model, are necessary to improve the understanding of CET. Such a study
5 was recently reported by Sakane *et al.* [53] for two-dimensional simulations and required the
6 use of GPU (Graphics Processing Units) supercomputers.
7

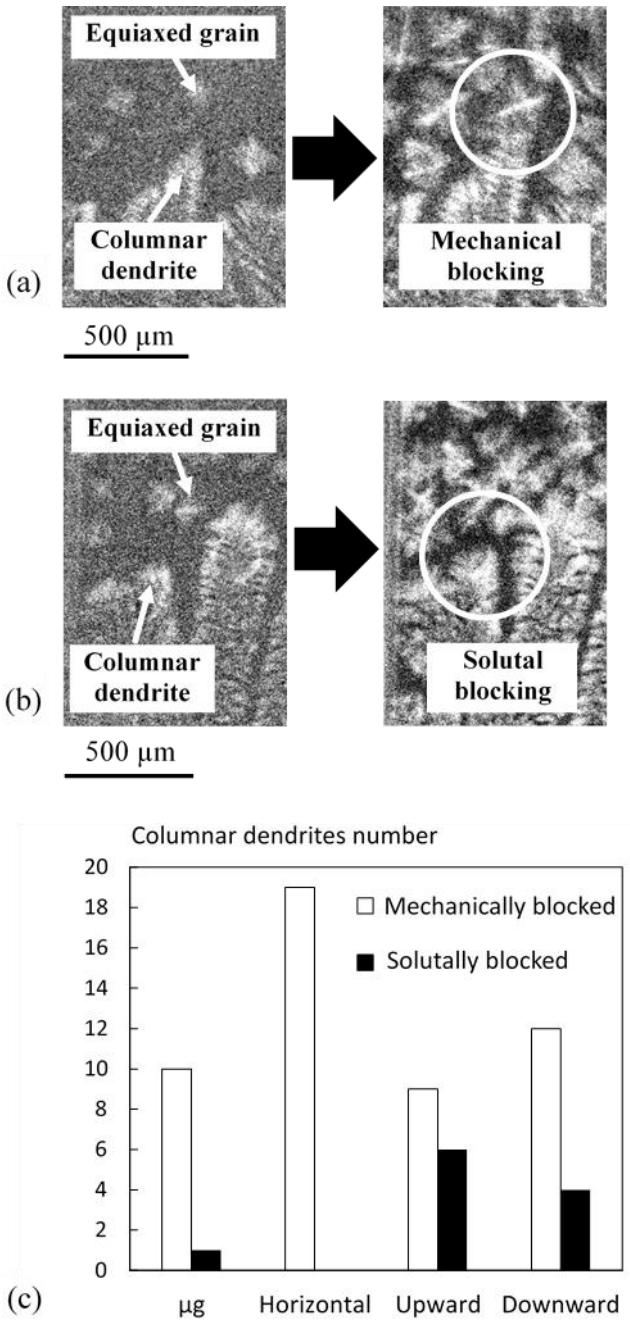

Fig.9: Radiographs illustrating (a) the mechanical blocking mechanism and (b) the solutal blocking mechanism. (c) Distribution of mechanical and solutal blocking for each solidification configuration.

4.3. Equiaxed grain structure after CET

The CET was followed by the propagation of an equiaxed front, as described in section 3.2 and in Soltani et al. [29]. The equiaxed grain structure was quantitatively characterised by measuring the grain size and the grain elongation factor defined in section 2.5. Distribution plots were obtained for these two parameters to determine the average value and the standard deviation. The results are summarised in Fig. 10 where the error bar corresponds to the standard deviation. Both the equiaxed grain size and elongation factor are very similar for all experiments. This was expected for the microgravity and horizontal experiments since gravity effects are removed or significantly reduced, respectively, in those cases. In the upward case, the shrinkage flow and the rapidly propagating equiaxed front prevent the grain motion after nucleation, leading to the development of a grain structure like the one obtained in microgravity and horizontal configuration. In a similar way for the downward case, the effective front propagation was much faster than solute sedimentation. Consequently, no solute plume developed during the equiaxed regime, and the equiaxed grain structure formation was not impacted. These observations confirm that gravity-related effects are reduced when increasing the solidification velocity [44].

Finally, it is worth noting that the grain elongation factor ϕ was about 1.3 for all experiments. According to Hunt's criterion, the grains can be considered as equiaxed ($\phi < 2$) [2], but the elongation factor did not reach unity even for the presently very high cooling rate, which means that the temperature gradient still had an influence on the grain development.

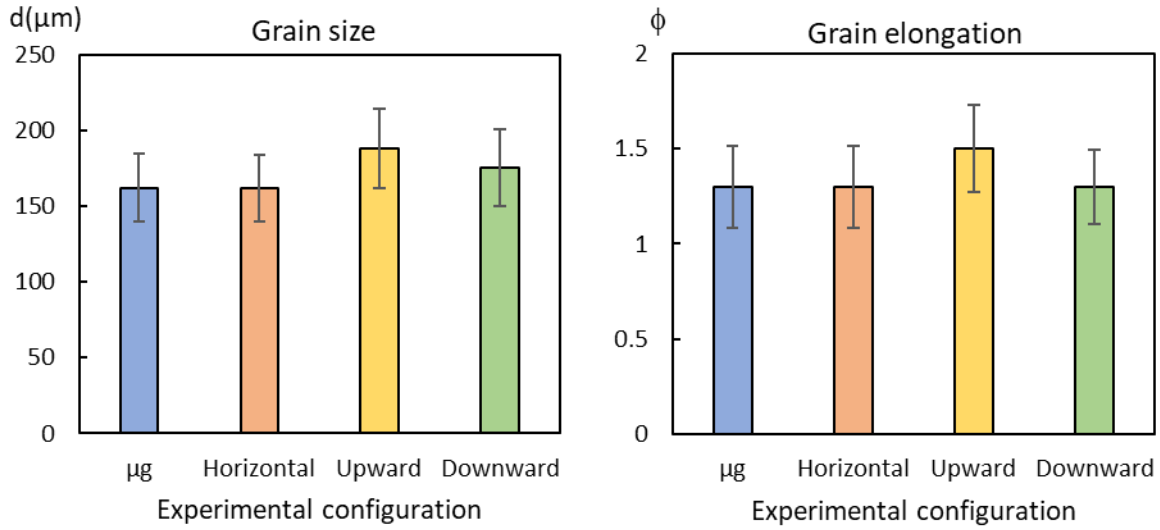

Fig.10: (a) Grain size distribution and (b) elongation distribution for the four investigated experiments.

5. Conclusion

The purpose of this study was to assess the impact of gravity-related effects on the Columnar-to-Equiaxed Transition in microgravity condition on board of the MASER-14 sounding rocket, and on Earth for three different experimental configurations: horizontal, vertical upward and vertical downward solidification. For each case, the different steps leading to a CET were observed *in situ* by using X-radiography. Analysis of the radiographs shows that the increase of the constitutional undercooling necessary to activate the refiners and induce the nucleation of the first grains could be attributed to the rapid decrease of the temperature after application of the rapid cooling rate. In the microgravity case, the nucleation distance is higher than in the three other experiments *i.e.*, equiaxed grains nucleated farther from the columnar dendrites. The low value of nucleation distance for ground experiments is attributed to

convective flow on Earth that reduces the solutal layer extent and leads to a shorter nucleation distance.

CET due to soft impingement by solutal interaction is prevalent in both vertically aligned solidification experiments. However, mechanical blocking, or hard impingement, is the dominant blocking mechanism in all experiments, due to the shrinkage flow that induces equiaxed grain motion toward the columnar dendrites. This observation highlights a significant importance of solidification-induced shrinkage flow, which is often overlooked. Further investigations on this subject would be worthy of interest, both experimentally for samples with similar geometry or bulk samples, and theoretically.

The analyses show that gravity did not impact the grain morphology and size in the equiaxed regime at very high cooling rate. The data collected during this campaign will thereafter be used as benchmark inputs for comparison with numerical simulations and theoretical models to improve the understanding the various processes occurring during CET in metal alloys.

Acknowledgements

This work was supported by the XRMON project (AO-2004-046) of the MAP program of the European Space Agency (ESA) and by the French National Space Agency (CNES). The authors would also like to thank the Swedish Space Corporation (SSC) for the development of the XRMON-GF2 facility and the technical support. We would also like to thank Antonio Verga

from ESA for his support and the fruitful discussions throughout the sounding rocket campaign.

Appendix A. Supplementary data

Supplementary data related to this article can be found at (link to supplementary material)

References

[1] J.A. Spittle, Columnar to equiaxed grain transition in as solidified alloys, Int. Mater. Rev. 51 (2006) 247–269. https://doi.org/10.1179/174328006X102493.

[2] J.D. Hunt, Steady state columnar and equiaxed growth of dendrites and eutectic, Mater. Sci. Eng. 65 (1984) 75–83. https://doi.org/10.1016/0025-5416(84)90201-5.

[3] M.A. Martorano, C. Beckermann, C.-A. Gandin, A solutal interaction mechanism for the columnar-to-equiaxed transition in alloy solidification, Metall. Mater. Trans. A. 34 (2003) 1657–1674. https://doi.org/10.1007/s11661-003-0311-x.

[4] D.R. Liu, N. Mangelinck-Noël, Ch.-A. Gandin, G. Zimmermann, L. Sturz, H. Nguyen-Thi, B. Billia, Simulation of directional solidification of refined Al–7wt.%Si alloys – Comparison with benchmark microgravity experiments, Acta Mater. 93 (2015) 24–37. https://doi.org/10.1016/j.actamat.2015.03.058.

[5] Y.Z. Li, N. Mangelinck-Noël, G. Zimmermann, L. Sturz, H. Nguyen-Thi, Effect of solidification conditions and surface pores on the microstructure and columnar-to-equiaxed transition in solidification under microgravity, J. Alloys Compd. 749 (2018) 344–354. https://doi.org/10.1016/j.jallcom.2018.03.300.

[6] Y.Z. Li, N. Mangelinck-Noël, G. Zimmermann, L. Sturz, H. Nguyen-Thi, Comparative study of directional solidification of Al-7 wt% Si alloys in Space and on Earth: Effects of gravity on dendrite growth and Columnar-to-equiaxed transition, J. Cryst. Growth. 513 (2019) 20–29. https://doi.org/10.1016/j.jcrysgro.2019.02.050.

[7] N. Shevchenko, O. Roshchupkina, O. Sokolova, S. Eckert, The effect of natural and forced melt convection on dendritic solidification in Ga–In alloys, J. Cryst. Growth. 417 (2015) 1–8. https://doi.org/10.1016/j.jcrysgro.2014.11.043.

[8] H. Nguyen-Thi, A. Bogno, G. Reinhart, B. Billia, R.H. Mathiesen, G. Zimmermann, Y. Houltz, K. Löth, D. Voss, A. Verga, F. de Pascale, Investigation of gravity effects on solidification of binary alloys with in situ X-ray radiography on earth and in microgravity environment, J. Phys. Conf. Ser. 327 (2011) 012012. https://doi.org/10.1088/1742-6596/327/1/012012.

[9] A.G. Murphy, W.U. Mirihanage, D.J. Browne, R.H. Mathiesen, Equiaxed dendritic

solidification and grain refiner potency characterised through in situ X-radiography, Acta Mater. 95 (2015) 83–89. https://doi.org/10.1016/j.actamat.2015.04.060.
[10] G. Reinhart, H. Nguyen-Thi, N. Mangelinck-Noël, J. Baruchel, B. Billia, In Situ Investigation of Dendrite Deformation During Upward Solidification of Al-7wt.%Si, JOM. 66 (2014) 1408–1414. https://doi.org/10.1007/s11837-014-1030-z.
[11] M. Cisternas Fernández, M. Založnik, H. Combeau, U. Hecht, Thermosolutal convection and macrosegregation during directional solidification of TiAl alloys in centrifugal casting, Int. J. Heat Mass Transf. 154 (2020) 119698. https://doi.org/10.1016/j.ijheatmasstransfer.2020.119698.
[12] L. Abou-Khalil, G. Salloum-Abou-Jaoude, G. Reinhart, C. Pickmann, G. Zimmermann, H. Nguyen-Thi, Influence of gravity level on Columnar-to-Equiaxed Transition during directional solidification of Al – 20 wt.% Cu alloys, Acta Mater. 110 (2016) 44–52. https://doi.org/10.1016/j.actamat.2016.03.007.
[13] H. Nguyen-Thi, G. Reinhart, G. Salloum Abou Jaoude, R.H. Mathiesen, G. Zimmermann, Y. Houltz, D. Voss, A. Verga, D.J. Browne, A.G. Murphy, XRMON-GF: A novel facility for solidification of metallic alloys with in situ and time-resolved X-ray radiographic characterization in microgravity conditions, J. Cryst. Growth. 374 (2013) 23–30. https://doi.org/10.1016/j.jcrysgro.2013.03.032.
[14] A.G. Murphy, R.H. Mathiesen, Y. Houltz, J. Li, C. Lockowandt, K. Henriksson, G. Zimmermann, N. Melville, D.J. Browne, XRMON-SOL: Isothermal equiaxed solidification of a grain refined Al–20 wt%Cu alloy, J. Cryst. Growth. 440 (2016) 38–46. https://doi.org/10.1016/j.jcrysgro.2016.01.032.
[15] S. Akamatsu, H. Nguyen-Thi, In situ observation of solidification patterns in diffusive conditions, Acta Mater. 108 (2016) 325–346. https://doi.org/10.1016/j.actamat.2016.01.024.
[16] G. Zimmermann, L. Sturz, H. Nguyen-Thi, N. Mangelinck-Noel, Y.Z. Li, C.-A. Gandin, R. Fleurisson, G. Guillemot, S. McFadden, R.P. Mooney, P. Voorhees, A. Roosz, A. Ronaföldi, C. Beckermann, A. Karma, C.-H. Chen, N. Warnken, A. Saad, G.-U. Grün, M. Grohn, I. Poitrault, T. Pehl, I. Nagy, D. Todt, O. Minster, W. Sillekens, Columnar and Equiaxed Solidification of Al-7 wt.% Si Alloys in Reduced Gravity in the Framework of the CETSOL Project, JOM. 69 (2017) 1269–1279. https://doi.org/10.1007/s11837-017-2397-4.
[17] B. Drevet, D. Camel, C. Malmejac, J.J. Favier, H. Nguyen Thi, Q. Li, B. Billia, Cellular and dendritic solidification of Al□Li alloys during the D2-mission, Adv. Space Res. 16 (1995) 173–176. https://doi.org/10.1016/0273-1177(95)00154-7.
[18] H. Nguyen Thi, Y. Dabo, B. Drevet, M.D. Dupouy, D. Camel, B. Billia, J.D. Hunt, A. Chilton, Directional solidification of Al–1.5 wt% Ni alloys under diffusion transport in space and fluid-flow localisation on earth, J. Cryst. Growth. 281 (2005) 654–668. https://doi.org/10.1016/j.jcrysgro.2005.04.061.
[19] R.H. Mathiesen, L. Arnberg, H. Nguyen-Thi, B. Billia, In Situ X-Ray Video Microscopy as a Tool in Solidification Science, JOM. 64 (2012) 76–82. https://doi.org/10.1007/s11837-011-0213-0.

[20] H. Nguyen-Thi, G. Reinhart, G. Salloum-Abou-Jaoude, D.J. Browne, A.G. Murphy, Y. Houltz, J. Li, D. Voss, A. Verga, R.H. Mathiesen, G. Zimmermann, XRMON-GF Experiments Devoted to the in Situ X-ray Radiographic Observation of Growth Process in Microgravity Conditions, Microgravity Sci. Technol. 26 (2014) 37–50. https://doi.org/10.1007/s12217-014-9370-4.
[21] G. Salloum-Abou-Jaoude, H. Nguyen-Thi, G. Reinhart, R.H. Mathiesen, G. Zimmermann, D. Voss, Characterization of Motion of Dendrite Fragment by X-Ray Radiography on Earth and under Microgravity Environment, Mater. Sci. Forum. (2014). https://doi.org/10.4028/www.scientific.net/MSF.790-791.311.
[22] H. Soltani, F. Ngomesse, G. Reinhart, M.C. Benoudia, M. Zahzouh, H. Nguyen-Thi, Impact of gravity on directional solidification of refined Al-20wt.%Cu alloy investigated by in situ X-radiography, J. Alloys Compd. (2020) 158028. https://doi.org/10.1016/j.jallcom.2020.158028.
[23] H. Nguyen-Thi, L. Salvo, R.H. Mathiesen, L. Arnberg, B. Billia, M. Suery, G. Reinhart, On the interest of synchrotron X-ray imaging for the study of solidification in metallic alloys, Comptes Rendus Phys. 13 (2012) 237–245. https://doi.org/10.1016/j.crhy.2011.11.010.
[24] C. Rakete, C. Baumbach, A. Goldschmidt, D. Samberg, C.G. Schroer, F. Breede, C. Stenzel, G. Zimmermann, C. Pickmann, Y. Houltz, C. Lockowandt, O. Svenonius, P. Wiklund, R.H. Mathiesen, Compact x-ray microradiograph for in situ imaging of solidification processes: Bringing in situ x-ray micro-imaging from the synchrotron to the laboratory, Rev. Sci. Instrum. 82 (2011) 105108. https://doi.org/10.1063/1.3650468.
[25] M. Becker, C. Dreißigacker, S. Klein, F. Kargl, Near-isothermal furnace for in situ and real time X-ray radiography solidification experiments, Rev. Sci. Instrum. 86 (2015) 063904. https://doi.org/10.1063/1.4922359.
[26] S. Boden, S. Eckert, B. Willers, G. Gerbeth, X-Ray Radioscopic Visualization of the Solutal Convection during Solidification of a Ga-30 Wt Pct In Alloy, Metall. Mater. Trans. A. 39 (2008) 613–623. https://doi.org/10.1007/s11661-007-9462-5.
[27] Y. Xu, D. Casari, Q. Du, R.H. Mathiesen, L. Arnberg, Y. Li, Heterogeneous nucleation and grain growth of inoculated aluminium alloys: An integrated study by in-situ X-radiography and numerical modelling, Acta Mater. 140 (2017) 224–239. https://doi.org/10.1016/j.actamat.2017.08.053.
[28] D.J. Browne, F. Garcia-Moreno, H. Nguyen-Thi, G. Zimmermann, F. Kargl, R.H. Mathiesen, A. Griesche, O. Minster, Overview of In Situ X-Ray Studies of Light Alloy Solidification in Microgravity, in: K.N. Solanki, D. Orlov, A. Singh, N.R. Neelameggham (Eds.), Magnes. Technol. 2017, Springer International Publishing Ag, Cham, 2017: pp. 581–590.
[29] H. Soltani, G. Reinhart, M.C. Benoudia, F. Ngomesse, M. Zahzouh, H. Nguyen-Thi, Impact of growth velocity on grain structure formation during directional solidification of a refined Al-20 wt.%Cu alloy, J. Cryst. Growth. 548 (2020) 125819.

https://doi.org/10.1016/j.jcrysgro.2020.125819.
[30] A. Buffet, H. Nguyen-Thi, A. Bogno, T. Schenk, N. Mangelinck-Noël, G. Reinhart, N. Bergeon, B. Billia, J. Baruchel, Measurement of Solute Profiles by Means of Synchrotron X-Ray Radiography during Directional Solidification of Al-4 wt% Cu Alloys, Mater. Sci. Forum. 649 (2010) 331–336. https://doi.org/10.4028/www.scientific.net/MSF.649.331.
[31] A.G. Murphy, R.H. Mathiesen, Y. Houltz, J. Li, C. Lockowandt, K. Henriksson, N. Melville, D.J. Browne, Direct observation of spatially isothermal equiaxed solidification of an Al–Cu alloy in microgravity on board the MASER 13 sounding rocket, J. Cryst. Growth. 454 (2016) 96–104. https://doi.org/10.1016/j.jcrysgro.2016.08.054.
[32] M.D. Abramoff, P.J. Magalhães, S.J. Ram, Image processing with ImageJ, Biophotonics Int. 11 (2004) 36–42.
[33] W.U. Mirihanage, L. Arnberg, R.H. Mathiesen, In-situ observation of transient columnar dendrite growth in the presence of thermo-solutal convection, IOP Conf. Ser. Mater. Sci. Eng. 33 (2012) 012033. https://doi.org/10.1088/1757-899X/33/1/012033.
[34] G. Reinhart, D. Grange, L. Abou-Khalil, N. Mangelinck-Noël, N.T. Niane, V. Maguin, G. Guillemot, Ch.-A. Gandin, H. Nguyen-Thi, Impact of solute flow during directional solidification of a Ni-based alloy: In-situ and real-time X-radiography, Acta Mater. 194 (2020) 68–79. https://doi.org/10.1016/j.actamat.2020.04.003.
[35] G. Zimmermann, C. Pickmann, M. Hamacher, E. Schaberger-Zimmermann, H. Neumann-Heyme, K. Eckert, S. Eckert, Fragmentation-driven grain refinement in directional solidification of AlCu10wt-% alloy at low pulling speeds, Acta Mater. 126 (2017) 236–250. https://doi.org/10.1016/j.actamat.2016.12.063.
[36] A.G. Murphy, D.J. Browne, Y. Houltz, R.H. Mathiesen, In situ X-ray observations of gas porosity interactions with dendritic microstructures during solidification of Al-based alloys, IOP Conf. Ser. Mater. Sci. Eng. 117 (2016) 012067. https://doi.org/10.1088/1757-899X/117/1/012067.
[37] T. Werner, M. Becker, J. Baumann, C. Pickmann, L. Sturz, F. Kargl, In situ observation of the impact of hydrogen bubbles in Al–Cu melt on directional dendritic solidification, J. Mater. Sci. 56 (2021) 8225–8242. https://doi.org/10.1007/s10853-020-05748-3.
[38] N.O. Young, J.S. Goldstein, M.J. Block, The motion of bubbles in a vertical temperature gradient, J. Fluid Mech. 6 (1959) 350–356. https://doi.org/10.1017/S0022112059000684.
[39] A.L. Greer, A.M. Bunn, A. Tronche, P.V. Evans, D.J. Bristow, Modelling of inoculation of metallic melts: application to grain refinement of aluminium by Al–Ti–B, Acta Mater. 48 (2000) 2823–2835. https://doi.org/10.1016/S1359-6454(00)00094-X.
[40] H. Nguyen-Thi, G. Reinhart, N. Mangelinck-Noël, H. Jung, B. Billia, T. Schenk, J. Gastaldi, J. Härtwig, J. Baruchel, In-Situ and Real-Time Investigation of Columnar-to-Equiaxed Transition in Metallic Alloy, Metall. Mater. Trans. A. 38 (2007) 1458–1464. https://doi.org/10.1007/s11661-007-9170-1.
[41] A. Prasad, S.D. McDonald, H. Yasuda, K. Nogita, D.H. StJohn, A real-time synchrotron X-ray study of primary phase nucleation and formation in hypoeutectic Al–Si alloys, J. Cryst. Growth. 430 (2015) 122–137. https://doi.org/10.1016/j.jcrysgro.2015.06.024.

[42] Y. Xu, D. Casari, R.H. Mathiesen, Y. Li, Revealing the heterogeneous nucleation behavior of equiaxed grains of inoculated Al alloys during directional solidification, Acta Mater. 149 (2018) 312–325. https://doi.org/10.1016/jactamat.2018.02.058.
[43] Y. Jia, H. Huang, Y. Fu, G. Zhu, D. Shu, B. Sun, D.H. StJohn, An in situ investigation of the solute suppressed nucleation zone in an Al-15 wt% Cu alloy inoculated by Al-Ti-B, Scr. Mater. 167 (2019) 6–10. https://doi.org/10.1016/j.scriptamat.2019.03.032.
[44] M.D. Dupouy, D. Camel, Effects of gravity on columnar dendritic growth of metallic alloys: flow pattern and mass transfer, J. Cryst. Growth. 183 (1998) 469–489. https://doi.org/10.1016/S0022-0248(97)00415-6.
[45] A. Bogno, H. Nguyen-Thi, G. Reinhart, B. Billia, J. Baruchel, Growth and interaction of dendritic equiaxed grains: In situ characterization by synchrotron X-ray radiography, Acta Mater. 61 (2013) 1303–1315. https://doi.org/10.1016/j.actamat.2012.11.008.
[46] CRC Handbook of Chemistry and Physics, Routledge CRC Press. (n.d.). https://www.routledge.com/CRC-Handbook-of-Chemistry-and-Physics/Rumble/p/book/9780367712600 (accessed July 7, 2021).
[47] J.P. Garandet, J.J. Favier, D. Camel, Solutal boundary layer concept and scaling analysis: two keys to segregation phenomena in melt crystal growth, J. Cryst. Growth. 130 (1993) 113–122. https://doi.org/10.1016/0022-0248(93)90843-L.
[48] A.J. Clarke, D. Tourret, Y. Song, S.D. Imhoff, P.J. Gibbs, J.W. Gibbs, K. Fezzaa, A. Karma, Microstructure selection in thin-sample directional solidification of an Al-Cu alloy: In situ X-ray imaging and phase-field simulations, Acta Mater. 129 (2017) 203–216. https://doi.org/10.1016/j.actamat.2017.02.047.
[49] M. Becker, S. Klein, F. Kargl, In-situ solute measurements with a laboratory polychromatic microfocus X-ray source during equiaxed solidification of an Al-Ge alloy, Scr. Mater. 124 (2016) 34–37. https://doi.org/10.1016/j.scriptamat.2016.06.032.
[50] S. Vernède, P. Jarry, M. Rappaz, A granular model of equiaxed mushy zones: Formation of a coherent solid and localization of feeding, Acta Mater. 54 (2006) 4023–4034. https://doi.org/10.1016/j.actamat.2006.04.035.
[51] A. Olmedilla, M. Založnik, B. Rouat, H. Combeau, Packing of sedimenting equiaxed dendrites, Phys. Rev. E. 97 (2018) 012910. https://doi.org/10.1103/PhysRevE.97.012910.
[52] A.K. Boukellal, J.-M. Debierre, G. Reinhart, H. Nguyen-Thi, Scaling laws governing the growth and interaction of equiaxed Al-Cu dendrites: A study combining experiments with phase-field simulations, Materialia. 1 (2018) 62–69. https://doi.org/10.1016/j.mtla.2018.04.008.
[53] S. Sakane, T. Takaki, M. Ohno, Y. Shibuta, T. Aoki, Two-dimensional large-scale phase-field lattice Boltzmann simulation of polycrystalline equiaxed solidification with motion of a massive number of dendrites, Comput. Mater. Sci. 178 (2020) 109639. https://doi.org/10.1016/j.commatsci.2020.109639.